Nuclear Inst. and Methods in Physics Research, A 983 (2020) 164522

Contents lists available at ScienceDirect

Nuclear Inst. and Methods in Physics Research, A

journal homepage: www.elsevier.com/locate/nima

The impact of synchrotron radiation at the Compact Linear Collider

D. Arominski [a,b,c,*,1], A. Sailer [a], A. Latina [a], D. Schulte [a]

[a] CERN, Geneva, Switzerland
[b] Warsaw University of Technology, Warsaw, Poland
[c] Institut Laue-Langevin, Grenoble, France

ARTICLE INFO

Keywords:
Synchrotron radiation
X-ray reflections
Machine–detector interface
CLIC

ABSTRACT

Synchrotron radiation (SR) emission and interactions with the vacuum chamber walls have the potential to negatively impact the performance of future electron–positron colliders. The Beam Delivery System (BDS) of the Compact Linear Collider (CLIC) contains weak bending and multipole magnets that lead to less intense emissions than at circular colliders with similar centre-of-mass energies. However, the linear geometry more easily allows for multiple reflections of SR photons, that can travel further downstream in the accelerator and impact the detector region. In this study, the results of PLACET and Synrad+ simulations of photon emissions and reflections in the CLIC BDS at two energy stages of 380 GeV and 3 TeV are presented. Estimates are given for heating and outgassing caused by SR photons interacting with the vacuum chamber in the BDS. The occupancy levels in the tracking detectors coming from full-detector simulations in GEANT4 are presented. Optimised beam pipe apertures are proposed for the forward detector region, as well as mitigation methods to ensure the safety and best possible performance of the detector.

1. Introduction

Synchrotron radiation (SR) is emitted by charged particles undergoing acceleration. This phenomenon is used in synchrotron light sources, such as ESRF [1], to study new materials, biological systems, and chemical reactions. However, in the scope of an electron–positron collider, the emission and reflections of the SR are detrimental effects that limit the machine performance. The power emitted in the form of SR is the main factor limiting the achievable energy and luminosity of circular colliders, such as the Large Electron–Positron Collider (LEP2) [2], the Future Circular Collider (FCC-ee) [3] or the Circular Electron–Positron Collider (CEPC) [4]. The photons can be a source of background in the detectors in both circular and linear colliders, for example in Stanford Linear Collider [5] as well as for the future machines, such as the International Linear Collider (ILC) [6] and the Compact Linear Collider (CLIC) [7].

The Compact Linear Collider (CLIC) is a proposed future electron–positron collider with the potential to reach centre-of-mass energies in the TeV scale. The construction and physics programme is assumed to be carried out in three stages: at 380 GeV, 1.5 TeV, and at 3 TeV centre-of-mass energy [8].

To achieve the desired high instantaneous luminosity at CLIC, small bunch sizes on the order of nanometres each with a population on the order of 10^9 particles are required [8]. The Beam Delivery System (BDS) transports electron and positron beams from the linacs to the Interaction Point (IP). First, the beam is cleaned in the energy and betatron collimation sections and then it is focused in the Final Focus System (FFS). The FFS is consists of dipoles, quadrupoles and sextupoles that have been optimised to match the desired beam parameters at the IP. The total FFS length is 770 m at both 380 GeV and 3 TeV, and its layout is shown in Fig. 1 [8].

The high energy of the electron and positron beams leads to the emission of a broad spectrum of synchrotron radiation, reaching MeV energies, in the bending and multipole magnets. These emissions are less intense than at circular colliders with similar centre-of-mass energies. However, the linear geometry and low grazing angles increase the probability of SR photons reflecting from the beam pipe surface and travelling further downstream into the detector region. These particles could leave significant energy deposits in the CLIC detector (CLICdet) [11] and therefore need to be studied carefully as a source of background that might degrade the detector performance.

The effect of SR photons on the detector is applicable both to the CLIC and ILC where their energy stages are comparable. This is due to similarities in the FFS and detector design. If SR were found to be an issue at 380 GeV CLIC, the subject should be studied for the ILC at both 250 GeV and 500 GeV.

The impact of SR photons on the vacuum quality and the detector has been studied for FCC-hh [12] and FCC-ee [13]. It was found to be a significant issue that requires mitigation in both machines. FCC-hh requires a saw-tooth pattern imprinted on the beam pipe surface

* Corresponding author at: Warsaw University of Technology, Warsaw, Poland.
E-mail address: arominski@ill.fr (D. Arominski).
[1] Now at: Institut Laue-Langevin, Grenoble, France.

https://doi.org/10.1016/j.nima.2020.164522
Received 14 July 2020; Accepted 5 August 2020
Available online 13 August 2020

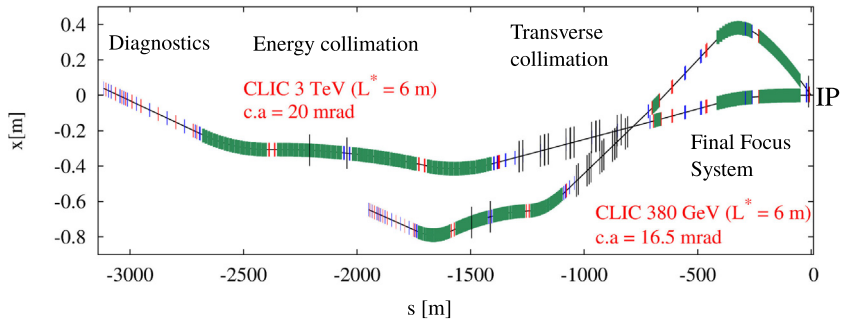

Fig. 1. CLIC Beam Delivery System layout at 380 GeV and 3 TeV split into four main sections. The Final Focus System (FFS) starts 770 m from the IP and is simulated in both PLACET and Synrad+. L^* is the distance between the final quadrupole of the FFS and the Interaction Point (IP), and c.a. denotes the crossing angle, that differs between the energy stages.

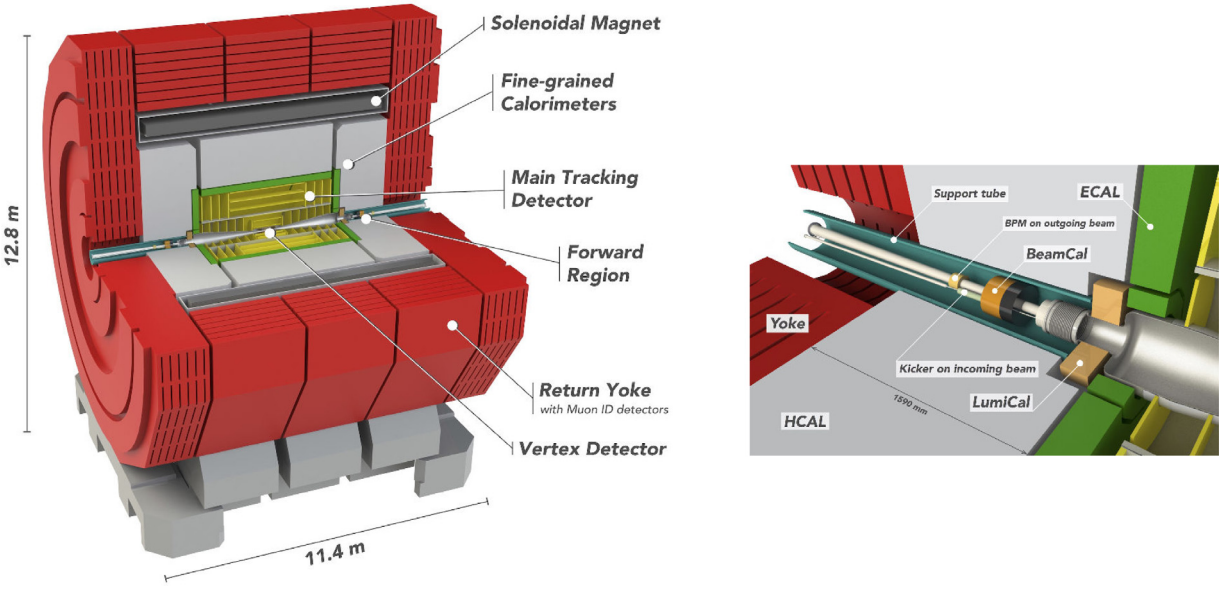

Fig. 2. Layout of the CLIC detector with major systems and subdetectors (a), and layout of the CLICdet forward region (b) [9].

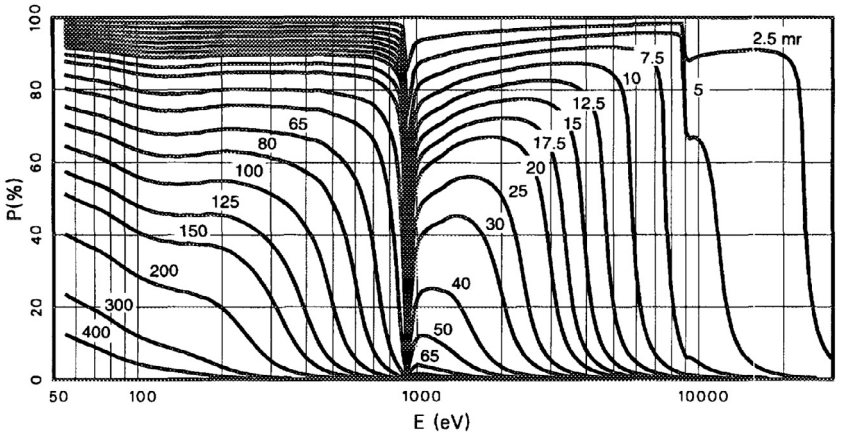

Fig. 3. Reflectivity of copper as a function of energy and grazing angle, from the Henke database [10].

as a part of the beam screen [14], and SR masks and shielding need to be installed in the detector region of FCC-ee experiments [12]. SR masks were also required to protect the experiments on the Large Electron–Positron Collider (LEP) [15,16].

CLICdet, shown in Fig. 2(a), is a design for a future multi-purpose detector, benefitting from the experiences of LEP and LHC experiments, and a robust R&D programme [9]. In the centre of the detector, immediately outside the beryllium beam pipe, is a silicon pixel Vertex detector with 25 μm × 25 μm sensors. Surrounding the Vertex detector is a tracker with larger silicon sensors (representative size 30 μm × 300 μm). SR can negatively impact the performance of both tracking detectors if photons end up in the acceptance of the detector, due to silicon detectors' low energy thresholds. In the forward detector region, shown in Fig. 2(b),

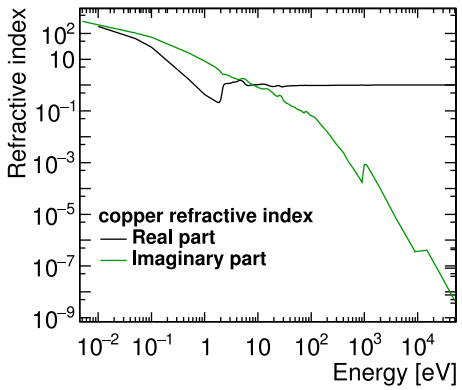

Fig. 4. Real and imaginary part of copper refractive index as a function of photon energy [17].

the incoming and outgoing beam pipes connect in the vicinity of the forward beam (BeamCal) and luminosity (LumiCal) calorimeters. Directly outside the yoke, 6 m from the interaction point is the final quadrupole QD0 of the FFS. More details on the detector layout and technology choices can be found in Refs. [9,11].

In this paper, the SR impact on both the CLIC BDS and detector regions at two energy stages, 380 GeV and 3 TeV is presented. First, simulation tools and analysis methods are introduced. Next, the impact of SR photons is studied in the CLIC BDS, followed by estimates of the temperature increase and outgassing rate in the beam pipe. The occupancies arising in the tracking detectors from SR photons are presented. Finally, the beam pipe apertures in the detector region are revisited and methods to mitigate the occupancies determined are discussed.

1.1. Photon interactions

Reflection is a common phenomenon for photons belonging to the visible spectrum; however, it can also take place for higher energy photons of up to about 30 keV [10]. The probability of reflection depends strongly on the incident angle, especially at the higher energy of the photon. Reflectivity distributions as a function of energy and grazing angle for copper are shown in Fig. 3. The minimum in reflectivity around the photon energy of 1 keV is caused by the proximity of the spectral L-lines of copper at 931 eV, 951 eV and 1096 eV [18].

There are two types of reflections considered in this study: specular, where the wavelength of a photon is much longer than the size of the imperfections of the reflective surface, and diffuse, where the wavelength is comparable with the surface roughness. In the former case, the incident angle is equal to the outgoing angle. In a diffuse reflection the outgoing angle has a distribution that depends on the surface properties, such as average roughness (R_a). Diffuse reflection can also lead to back-scattering of photons.

The scattering factors can be obtained from the Henke database [10] and the refractive indices for many materials are available in the Refractive Index Database [19]. An example of a distribution of the refractive index of copper is shown in Fig. 4.

2. Simulation treatment

Simulations of the synchrotron radiation effects are performed using PLACET [20] and Synrad+ [21]. PLACET is used to obtain information regarding the total emitted power along the BDS, and the location of the SR emissions. The emitted SR photons are not tracked in the code. Thus, the photon interactions with the vacuum chamber are not studied with PLACET, and Synrad+ is used instead. The energy and angular spectra of the emitted photons show good agreement between the predictions of PLACET and Synrad+. The CLIC FFS is implemented in Synrad+ and the SR created along the accelerator are tracked until they reach the exit aperture of the QD0 or BeamCal. The photon impact on the CLICdet is studied in full-detector simulations using Geant4 [22].

A special version of the PLACET code is prepared, where more information about the SR is made available to the user. In the base version, PLACET includes the SR effects in the form of energy loss of the particle moving through bending, quadrupole, and multipole magnets. In the adapted version, the energy loss is translated into SR photons. The initial position and direction of a photon momentum is the same as the direction of the particle from which it was emitted. The photons inherit their angular distribution from the emitting particles, as PLACET does not provide the information of the direction of the trajectory change due to the SR emission.

In a second step, Synrad+ is used for the treatment of the SR reflections in the CLIC Final Focus System. The photon reflection probabilities are calculated using the Synrad3D implementation [23]. The entire BDS is not simulated in Synrad+, but only the FFS, as the additional length of the accelerator upstream the FFS significantly slows down the computations, without providing additional insight into the SR impact on the detector region. Most of the photons emitted in the BDS cannot reach the detector region without undergoing multiple interactions with the vacuum chamber wall surface that make it highly unlikely for them to travel to the IP. Therefore, omitting the photons produced prior to the FFS does not affect the results at the IP in a significant way.

The geometry of the simulated system is built using software external to Synrad+, that takes as input a MAD-X [24] survey output file with the parameters of the accelerator lattice, and creates a geometry readable by Synrad+. The information regarding magnetic regions of sector bending and quadrupole magnets is recorded, and put in the context of the aperture model. The apertures of the magnets can be inserted directly, while the radii of the vacuum chamber in the drifts are interpolated as a linear transition between the apertures in the nearest magnetic regions.

Several types of materials provided with Synrad+ are used in the simulations of the CLIC FFS, namely: copper, iron, as well as some hypothetical materials such as the perfect absorber and more complicated shapes such as saw-tooth.

The perfect absorber material is used first to establish the impact of direct photons on the detector that can be compared with PLACET results, where the photon reflections are not included. This material is also used to obtain information regarding the power emitted in the last few bending magnets and the final doublet that is carried by the SR photons entering the detector region.

Subsequently, copper and iron are used to study the impact of realistic reflectivities on the photon distributions at the QD0 aperture. In this case, iron approximates the stainless steel that is foreseen as the main material of the beam pipe for the CLIC BDS (with copper-coating inside). The impact of small differences in reflectivity between the application of copper and iron as the material for the CLIC BDS vacuum chamber is analysed. Different average roughnesses are applied, with three main values of R_a used: 10 nm, 100 nm and 1 μm. The 100 nm average roughness is required in the CLIC main linac [25], with precision machining reaching down to 10 nm [26]. However, the FFS may not need to have such stringent requirements regarding the surface roughness, therefore several R_a values ranging from 1 μm down to 10 nm are studied to establish the sensitivity to different parameters and the related change in the photon flux and distributions at the QD0 exit.

The saw-tooth shape is used in the mitigation section. However, the computation cost of using a geometrically accurate saw-tooth is too high [27]. Therefore, a surface producing the same effect as the saw-tooth used in the LHC beam screen [28] is used in the simulations.

Photons are tracked in Synrad+ up to the exit of the QD0 (at 380 GeV and 3 TeV) or the exit of the BeamCal (only at 3 TeV). Then, for each photon the three-dimensional position, the four-momentum

vector and flux are stored for further analysis. Each stored photon has a flux attached to it, making it a macroparticle (macrophoton) that represents a number of 'real' photons. The flux depends on the beam current and the magnetic region properties. It can be reduced during reflections, where only a fraction of the flux interacting with the beam pipe material is reflected. The photon flux is equivalent to a number of 'real' photons a stored macrophoton represents, as well as the number of times the same macrophoton is embedded in the detector simulation.

The weight attached to each macrophoton is reduced in the procedure of normalising the results to one bunch train. First, the simulation time has to be taken into account. The simulations run for a longer time than 1 s to obtain the required statistics of macrophotons. The fluxes attached to each macrophotons are given per second, thus all collected macrophoton fluxes need to be divided by the simulation running time provided by Synrad+. Then, the assumption in Synrad+ that the beams represent a continuous current needs to be corrected. The bunch train time is used to multiply the flux attached to each photon, and is calculated as the time of a single bunch train passage.

Hit distributions are defined in the XY-plane, where the Z-axis is colinear with the longitudinal detector axis were obtained from Geant4 detector response. To account for photons coming from the second FFS, a hit distribution mirrored around Y-axis is added to its original distribution. A safety factor of two is used for photons to take into account the uncertainty in simulating the SR photon interactions with the material of the detector.

The main figure of merit is the occupancy level in the CLIC detector caused by the SR photons. All of the considered material choices and roughnesses are compared in terms of the energy of the photons that are in the acceptance of the detector, further called 'visible energy'. Out of these, a few representative examples are chosen for full detector simulations. The energy of a photon is recorded as visible if the photon has energy above 1 keV and a polar angle $\theta_{\mathrm{QD0}} > 3.3$ mrad. The polar angle is calculated from the centre beam axis at the exit of the QD0. The 3.3 mrad corresponds to the BeamCal aperture of 32 mm located on the opposite side of the detector. The occupancies are calculated according to Eq. (1).

The definition of occupancy used in silicon trackers follows the example used in Ref. [29,30] and is based on the background hit density per bunch train, which is scaled up by assumed clustering effects and safety factors:

$$O_{\mathrm{train}} = \sum_{\mathrm{background}} \rho_{\mathrm{Hits/BX}} \cdot n_{\mathrm{bunches/train}} \cdot p \cdot c \cdot sf_{\mathrm{background}}, \quad (1)$$

where:

- $\rho_{\mathrm{Hits/BX}}$ — density per mm^2 of hits above the threshold of 3.2 keV for 50 μm thick silicon sensors, and 6.4 keV for 100 μm sensors [31];
- p — sensor pitch, 25 μm × 25 μm in the Vertex and 300 μm × 30 μm in the Tracker [9];
- c — clustering factor, 5 for pixel sensors, 3 for other;
- sf — safety factor, assumed to be 2.

The energy deposited by background particles will lead to the releasing of free charge carriers in the silicon volume. As these charges migrate towards the minimum of electric potential at a readout, they spread laterally and charge sharing occurs, leading to the formation of clusters of one or more hit pixels. The exact cluster size depends on the sensor geometry, angular and momentum distribution of the incident particle and the design of the readout system. In this study, an approximate value of five for the pixel sensors and of three for the sensors in the trackers are assumed, in line with the values used in the previous beam-induced backgrounds study [31].

3. Impact in the BDS

3.1. Heating of the beam pipe

The power emitted in the form of SR heats up the beam pipe and can create conditions that require a dedicated cooling system to protect the accelerator components. The SR heating can be a problem especially in cryogenic systems, where the extraction of the unwanted heat is inefficient due to low efficiency of the Carnot cycle for systems with low temperature difference [32]. Heating of superconducting elements can lead to loss of superconductivity, and for example, magnet quenches. The cooling can also be required for normal-conducting elements if the heat load is deemed too high.

The total power emitted in the form of the SR photons in the BDS estimated using PLACET is 16 W at 380 GeV and 2.3 kW at 3 TeV, of which 11.4 W and 442 W, respectively, are emitted in the FFS. The numbers concerning the FFS can be compared between PLACET and Synrad+. Synrad+ predicts that the total power loss to SR is 11.2 W at 380 GeV and 332 W at 3 TeV. The results at 380 GeV are in excellent agreement, with less than 3% relative difference between the codes. The situation is different at 3 TeV, where the relative discrepancy reaches 33%. However, the difference can be explained by the photon top energy cut off at 50 MeV present in Synrad+ simulations. When the same energy range is imposed on the PLACET spectrum, the total emitted power is reduced to 367 W in the FFS, and the relative difference shrinks to about 10%. The remaining discrepancy is due to a more realistic beam representation in PLACET, where the energy spread and non-linear beam dynamics are taken into account. The PLACET prediction of the total power is used, as it is free from energy spectrum limitations present in the Synrad+ simulation.

The energy emitted in the form of the SR radiation along the CLIC BDS simulated with PLACET is shown in Fig. 5. From the detector perspective, the most significant SR emissions take place in the final doublet quadrupoles at both energy stages, due to the proximity of the emission point and the high energy carried by photons. However, in terms of the total emitted power, the photons emitted in the bending magnets in the last 400 m of the FFS are more relevant at both energy stages. These photons become especially relevant when the SR reflections are included in simulations. At 380 GeV 70% of the power is emitted in the FFS, while at 3 TeV it is only 20%, due to intense emissions in the collimation section. The average linear power densities at 380 GeV are 8 mW/m in the entire BDS and 14 mW/m in the FFS, increasing to 0.7 W/m and 0.6 W/m, respectively, at 3 TeV.

To allow an estimate the impact of the SR heat several assumptions are made: adiabatic conditions; an average beam pipe aperture of 15 mm at 380 GeV and 6 mm at 3 TeV with a uniform thickness of 1 mm, and instantaneous heating of the entire beam pipe element. The structure of the CLIC beam pipe consists of iron that is copper-coated on the inner surface. This coating is neglected in the following estimates. Using these assumptions, the temperature increase due to SR at each point of the distributions shown in Fig. 5 can be calculated using:

$$\Delta T = \frac{P_{\mathrm{SR}} \Delta t}{V \rho \sigma_{\mathrm{Fe}}}, \quad (2)$$

where: P_{SR} — SR power at given point, Δt — elapsed time, V — volume of the beam pipe material per bin length, ρ — density of iron, 7.87 $\frac{\mathrm{g}}{\mathrm{cm}^3}$ [18], σ_{Fe} — specific heat of iron, 0.449 $\frac{\mathrm{J}}{\mathrm{g\,K}}$ [18].

The temperature increase distribution along the BDS at both energy stages is shown in Fig. 6. In the calculation of the temperature increase per hour, no cooling or heat dissipation are assumed. In addition, complete absorption of the entire SR power is assumed at the point of emission. In the actual machine, the SR power will be more distributed along the accelerator, reducing the maximal temperature at any point.

The maximal temperature increase over the ambient temperature in the accelerator tunnel per hour at 380 GeV is just below 0.7 K. At 3 TeV, the temperature increase is substantially larger, leading to an unacceptable increase in the collimation region of up to 80 K/h. The temperature increase at the very end of the BDS is related to the SR emission in the final doublet. This energy is safely removed from the detector region and is not deposited in the beam pipe in the detector region, therefore it can be safely neglected when only the incoming beamline is considered. The temperature increase at 3 TeV needs to

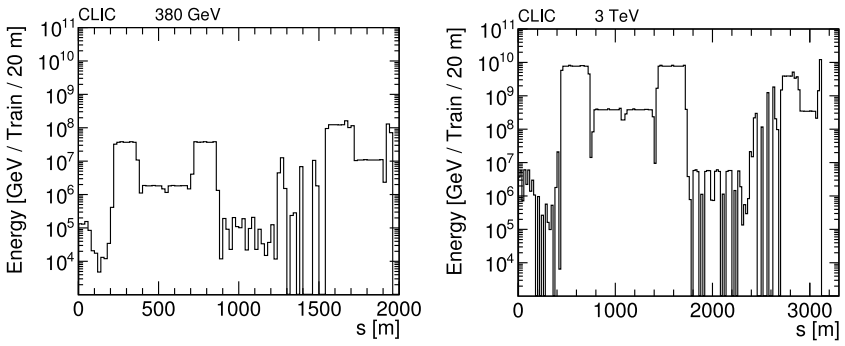

Fig. 5. Distributions of energy emitted in the form of synchrotron radiation photons along the CLIC BDS per bunch train at 380 GeV (a) and 3 TeV (b) simulated in PLACET.

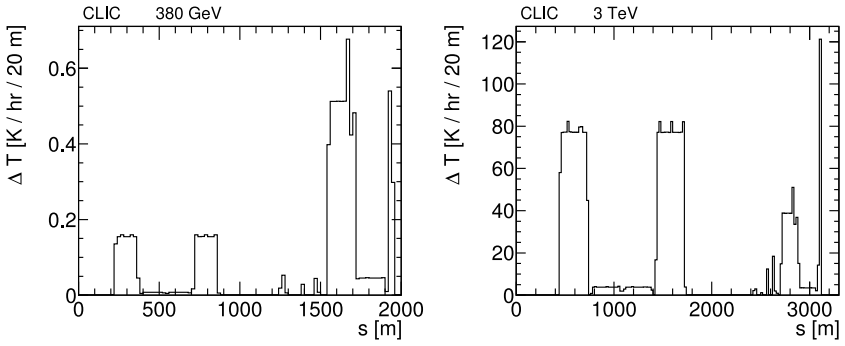

Fig. 6. Distributions of the temperature increase due to absorption of synchrotron radiation energy over one hour of machine running at 380 GeV (a) and 3 TeV (b). No power dissipation into ambient air or cooling is assumed.

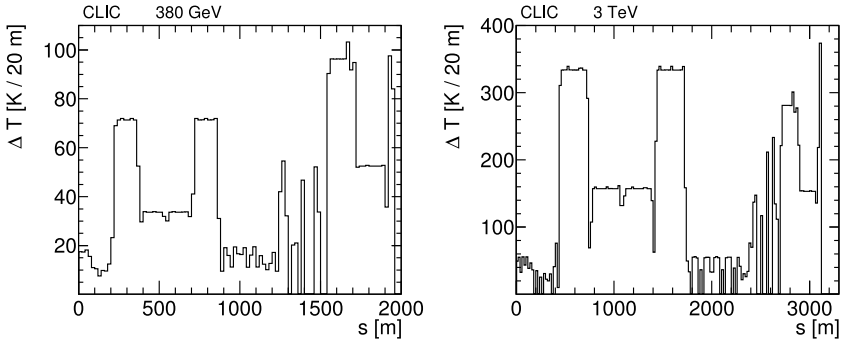

Fig. 7. Distributions of the equilibrium temperature increase above the ambient temperature at 380 GeV (a) and 3 TeV (b), assuming radiative cooling with 0.1 emissivity.

be addressed by a dedicated active cooling solution, while at 380 GeV active cooling may not be required.

Either passive or active cooling can be envisaged to address the heat load. First, let us estimate the efficiency of radiative and convective cooling, by calculating the equilibrium temperature difference between the beam pipe outer wall and the tunnel air.

The power emitted by the beam pipe at a temperature T_{pipe} in a tunnel with a temperature T_{ambient}, assuming a grey-body radiation, follows the Stefan–Boltzmann formula:

$$P = \varepsilon A \sigma_{\text{SB}} (T^4_{\text{pipe}} - T^4_{\text{ambient}}), \tag{3}$$

where: P — radiated power, ε — material emissivity: 0.1–0.94 for iron [33], A — emitting surface, $\sigma_{\text{SB}} = 5.67{\times}10^{-8}\ \frac{\text{W}}{\text{m}^2\text{K}^4}$ — Stefan–Boltzmann constant, T_{ambient} — air temperature in the tunnel surrounding the beam pipe, assumed to be 293 K.

In the equilibrium condition, the power received from the SR and emitted in the radiative cooling are equal, thus allowing one to calculate the equilibrium temperature difference using Eq. (4).

$$T_{\text{pipe}} = \left(\frac{P_{\text{SR}}}{\varepsilon A \sigma_{\text{SB}} + T^4_{\text{ambient}}} \right)^{1/4}. \tag{4}$$

This results in the maximum temperature increase in the range from 100 K at 380 GeV to 340 K at 3 TeV. Even if the a very high emissivity of 0.94 is assumed, the beam pipe would heat up by about 60 K above the ambient temperature at 380 GeV and 200 K at 3 TeV. Such a temperature rise is not acceptable, given the strict precision and stability requirements of the elements at the micrometre-level and the impact of the thermal expansion of the beampipe.

The equilibrium temperature along the BDS, when radiative cooling with 0.1 emissivity is assumed is shown in Fig. 7. The radiative cooling at both energy stages is not a viable choice, as it requires substantial temperature differences between the beam pipe and the ambient temperature. At 3 TeV, the temperature increase reaches up to 340 K in the collimation region, an increase that cannot be allowed due to the expected damages of the accelerator components. Therefore, radiative cooling is not sufficient to stabilise the beam pipe temperature, in particular not in the regions where the SR emission is the highest.

The other method to cool the beam pipe is by convection. Convective heat transfer is a complex phenomenon that depends on the

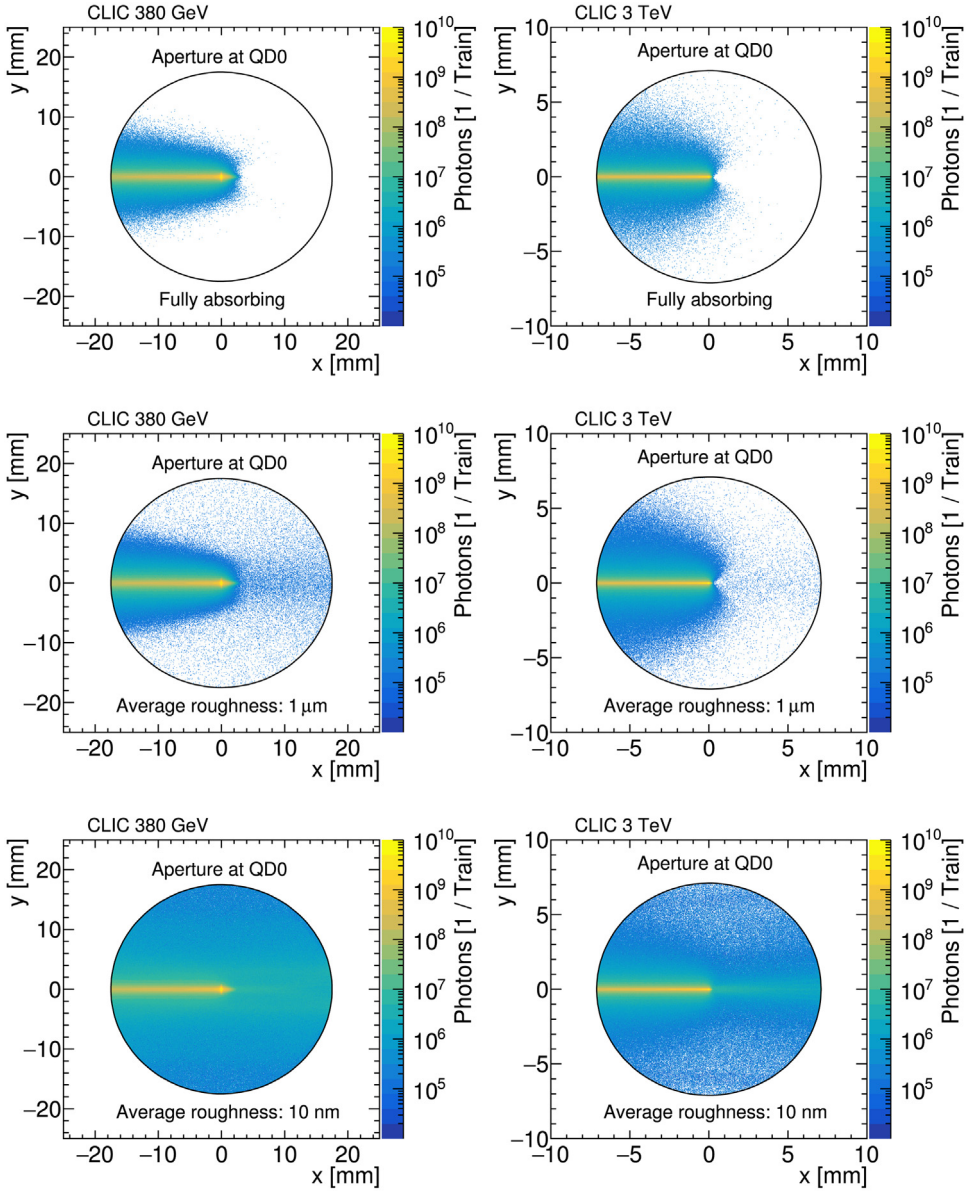

Fig. 8. Transverse position distributions of synchrotron radiation photons at the QD0 exit at 380 GeV (left column) and 3 TeV (right column) assuming fully absorbing walls (top), copper walls with 1 µm roughness (middle), copper walls with 10 nm roughness (bottom).

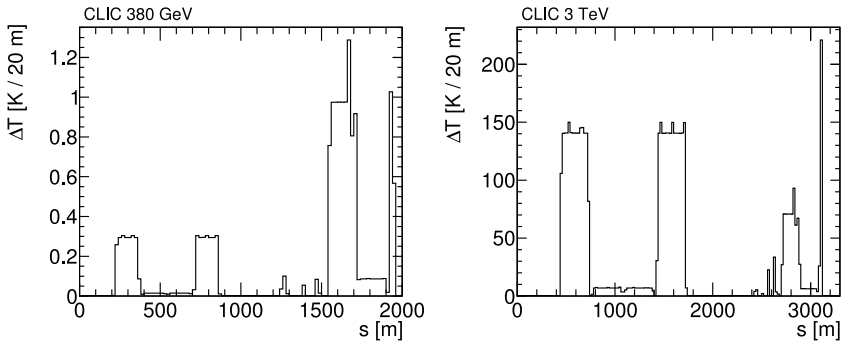

Fig. 9. Distributions of the equilibrium temperature increase at 380 GeV (a) and 3 TeV (b) assuming convective cooling with heat transfer coefficient $h = 0.5\ \frac{\mathrm{W}}{\mathrm{Km}^2}$.

shape of the heat-emitting object and the surrounding environment conditions. The exact description of this process is beyond the scope of this work, therefore a simplified approach to estimate the natural convection cooling of a beam pipe is used. The following equation describes the general expression for the convection heat exchange:

$$P = hA\Delta T, \tag{5}$$

where: h — heat transfer coefficient, A — area of the emitting surface, ΔT — temperature difference between the emitting surface and the surrounding environment.

For free (natural) laminar convection of air under normal pressure, the heat transfer coefficient varies from 0.5 $\frac{W}{Km^2}$ to 1000 $\frac{W}{Km^2}$ [34]. The lower value is used as a conservative estimate. To obtain the increase of the beam pipe temperature in the equilibrium condition, the heat transferred to air in the laminar convection must be equal to the power received from the SR:

$$\Delta T = \frac{P_{SR}}{hA}. \tag{6}$$

The equilibrium temperature difference when the convective cooling, with a heat transfer coefficient of 0.5 is assumed, is shown in Fig. 9. Convective cooling, even with such a low heat transfer coefficient, is sufficient to maintain the beam pipe temperature within 1 K of the ambient temperature at 380 GeV. At 3 TeV, the temperature increase is up to 150 K in the collimation region. The heat exchange coefficient needs to be at least 80 $\frac{W}{Km^2}$ to maintain the temperature increase due to SR heating within 1 K from the ambient temperature.

In conclusion, at 380 GeV, the average power of the synchrotron radiation is low, and the associated temperature rise under the assumed conditions is negligible. The situation is different at 3 TeV, where the average power per metre is about 90 times larger. The estimate of passive cooling efficiencies shows a substantial increase in the beam pipe temperature. Therefore, a dedicated cooling system for the beam pipes in the CLIC BDS at 3 TeV should be studied in more detail in the future, especially for the collimation region.

3.2. Photo-desorption and outgassing

Synchrotron radiation photons can cause significant photo-desorption, and the increased outgassing leads to a pressure rise in the vacuum system. It is the main source of the gas load in electron–positron storage rings such as LEP [35] or FCC-ee [36], and is also a major concern for the LHC vacuum system [37]. The synchrotron radiation reflections increase the area impacted by photons and thus increase the outgassing rates in the CLIC BDS.

The outgassing rate due to the synchrotron radiation desorption, assuming only the photo-electric effect, is defined as [37]:

$$Q'\,[\mathrm{mbar}\cdot\mathrm{l/s}] = K\eta\Gamma, \tag{7}$$

where: η — desorption yield ($2\cdot10^{-6}$ molecule/photon [36]), K — conversion from molecules to pressure ($4.01\cdot10^{-20}$ mbar·l/molecule at 298 K), Γ — photon yield (photons/s)

To maintain the average pressure $\langle P\rangle$ an effective pumping pressure S' is required:

$$S'[\mathrm{l/s}] = Q'/\langle P\rangle, \tag{8}$$

where: Q' is defined as in Eq. (7), and $\langle P\rangle$ is $2\cdot10^{-9}$ mbar in order to limit the beam losses to 10^{-5} [25].

The photon fluxes, corresponding gas loads, and required pumping speeds are summarised in Table 1. The photon fluxes are determined using Synrad+ simulations, using copper vacuum chamber walls with an average roughness of 100 nm and no SR absorbers. The results obtained for FCC-ee are quoted per length in the arcs, therefore the CLIC values from the FFS are made comparable by extracting average flux per metre. The maximal fluxes and outgassing loads provided by Synrad+ are given per square metre.

The photon fluxes and outgassing rates are more significant at 380 GeV than at 3 TeV. The photon emissions are more intense at the lower energy stage due to the higher beam current and a factor of two stronger weak bending magnets in the Final Focus System.

The maximal photon fluxes per area in the CLIC BDS are located directly in front of the QD0 entrance. The averages are estimated using the total number of absorbed photons along the FFS divided by the total length of the system. The average and maximal pumping speeds required in the CLIC FFS can be easily met with the planned use of Non-Evaporative Getter (NEG) pumps [25].

Table 1
Comparison of maximum and average outgassing loads in the CLIC FFS simulated with Synrad+ and FCC-ee [36] due to the photo-desorption.

	Photon flux [ph/s/m^i]	Gas load [mbar l/s/m^i]	Pumping speed [l/s/m^i]
CLIC 380 GeV max	3.6×10^{16}	2.9×10^{-9}	1.5
CLIC 380 GeV average	1.4×10^{12}	1.1×10^{-13}	5.5×10^{-5}
CLIC 3 TeV max	6.5×10^{15}	5.2×10^{-10}	2.6×10^{-1}
CLIC 3 TeV average	7.2×10^{11}	5.8×10^{-14}	2.9×10^{-5}
FCC-ee 91.2 GeV	7.1×10^{17}	5.7×10^{-8}	28.7
FCC-ee 365 GeV	1.2×10^{16}	9.5×10^{-10}	4.7×10^{-1}

$i = 1$ for FCC-ee and CLIC average data, while $i = 2$ for the maximal fluxes of photons interacting with vacuum chamber in the CLIC FFS.

Table 2
Beam pipe apertures in the detector region implemented in the simulation model for the 380 GeV energy stage based on the CLICdet model [11].

Beampipe[A]	Z_1 [mm]	Z_2 [mm]	R_1^{In} [mm]	R_2^{In} [mm]	R_1^{Out} [mm]	R_2^{Out} [mm]
0	0	308	29.4	29.4	30.0	30.0
0	308	337	29.4	29.4	30.0	33.4
0	337	2 080	29.4	235.2	33.4	240.0
0	2080	2 528	235.2	235.2	240.0	240.0
0[B]	2528	2 531	0.0	98.0	240.0	240.0
2	2531	3 170	98.0	98.0	99.0	99.0
2[C]	3170	3 173	17.5	31.0	99.0	99.0
2	3173	3 500	31.0	31.0	32.0	32.0
2[D]	3500	12 500	31.0	125.0	32.0	127.0
1	3173	3 281	17.5	17.5	18.5	18.5
1	3281	3 835	17.5	17.5	18.5	18.5
1	3835	3 845	17.5	17.5	18.5	18.5
1	3845	12 500	17.5	17.5	18.5	18.5

Each element has a circular aperture and is a cylindrical barrel or a cone located between Z_1 and Z_2. The radii $R_{1,2}^{In,Out}$ are the inner and outer radii at positions Z_1 and Z_2, respectively.
[A] Alignment of the beam pipe element: 0 — aligned on the detector axis, 1 — aligned on the incoming beam axis, 2 — aligned on outgoing beam axis.
[B] Beam pipe end in front of LumiCal: R_1^{Out} is the size of the hole where the beam pipe inside LumiCal is connected. The hole is centred on the outgoing beam axis.
[C] Beam pipe end in front of BeamCal: R_1^{In} is the size of the hole for the incoming beam pipe,
R_1^{Out} is the size of the hole for the outgoing beam pipe.
[D] Conical beam pipe with a half-opening angle of 10 mrad.

The SR-induced outgassing was found [36] to be a challenging issue that needs to be addressed at FCC-ee, while at CLIC the outgassing rates in the FFS are not significant. The maximal outgassing rate is at 380 GeV, and remains a factor ten below the average level of FCC-ee at 91.2 GeV (Z-boson pole). The required average and maximum pumping speeds in CLIC FFS are below the FCC-ee in the arcs at the Z-pole and do not constitute a threat to the quality of the vacuum system.

4. Impact in the detector region

Synchrotron radiation at CLIC can also be an issue in the detector region. Photons with energies surpassing 1 keV can penetrate the beam pipe and leave significant energy deposits in the sensitive material of the detector, especially in the Vertex and Tracker. SR photon background hits in the detector are discussed in the following.

First, the transverse photon distributions at the exit of the QD0 magnet are studied, and their impact on the beam pipe aperture choice in the detector region is discussed in Section 4.1. The impact of the vacuum chamber material on the photon polar angle and energy distributions is shown in Section 4.2. Finally, the hit densities and related occupancy levels in the tracking detectors are presented in Section 4.3.

4.1. Beam pipe aperture optimisation in the detector region

The apertures of the incoming beam pipe in the BeamCal region need to be optimised at both the 380 GeV and 3 TeV energy stages to

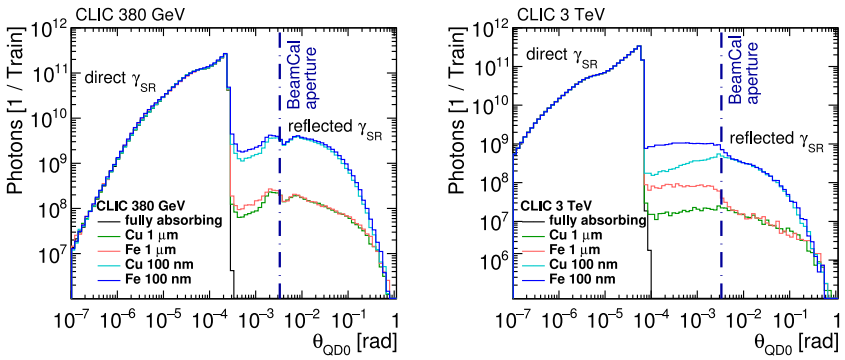

Fig. 10. Polar angle distributions of synchrotron radiation photons at the QD0 exit at 380 GeV (a) and 3 TeV (b) with copper and iron vacuum chamber walls with 1 μm and 100 nm average surface roughness simulated with Synrad+ [38]. θ_{QD0} signifies the polar angle where the reference point is located in the centre of the beampipe at the QD0 exit, 6 m upstream from the IP. The marked BeamCal aperture refers to the outgoing beam pipe radius in the BeamCal located on the opposite side of the detector.

Table 3
Beam pipe apertures in the detector region implemented in the simulation model for the 3 TeV energy stage.

Beampipe[A]	Z_1 [mm]	Z_2 [mm]	R_1^{In} [mm]	R_2^{In} [mm]	R_1^{Out} [mm]	R_2^{Out} [mm]
0	0	308	29.4	29.4	30.0	30.0
0	308	337	29.4	29.4	30.0	33.4
0	337	2 080	29.4	235.2	33.4	240.0
0	2080	2 528	235.2	235.2	240.0	240.0
0[B]	2528	2 531	0.0	98.0	240.0	240.0
2	2531	3 170	98.0	98.0	99.0	99.0
2[C]	3170	3 173	17.5	31.0	99.0	99.0
2	3173	3 500	31.0	31.0	32.0	32.0
2[D]	3500	12 500	31.0	125.0	32.0	127.0
1	3173	3 281	7.6	7.6	8.6	8.6
1	3281	3 835	7.6	7.6	8.6	8.6
1	3835	3 845	7.6	7.6	8.6	8.6
1	3845	12 500	7.6	7.6	8.6	8.6

The parameter descriptions are the same as for the 380 GeV design in Table 2. [11].

Table 4
The energy carried by photons with polar angle $\theta_{QD0} > 3.3$ mrad per bunch train, dubbed 'visible energy', for various assumptions on the beam pipe material and its roughness. The energy that can be deposited in the detector is two times larger than the presented numbers, as two beamlines meet in the interaction region. Safety factors are not included.

	Visible energy [TeV]	
	380 GeV	3 TeV
Fully absorbing	0.0	0.0
Cu 1 μm	7.0	0.9
Fe 1 μm	8.6	50
Cu 100 nm	85	11
Fe 100 nm	1.2×10^2	6.0×10^2
Cu 10 nm	3.9×10^2	1.1×10^2
Fe 10 nm	6.0×10^2	3.7×10^3

take into account the transverse SR photons distributions. The SR photons transverse position distributions at the exit of the QD0 with fully absorbing walls of the vacuum chamber and two roughness options for copper are shown in Fig. 8. Photons are concentrated centrally and along the X-axis. In all cases, the photons around the centre originate mainly from the final doublet, while the elongated distribution along the X-axis originates from emissions in the last few bending magnets. The photons with positive X position are predominantly due to reflections from the vacuum chamber walls in the FFS. Higher reflectivity of the vacuum chamber walls leads to photons filling out the entire available transverse space of the QD0 aperture [38].

It is a design requirement that the photons emitted in the final quadrupole doublet do not interact with the material of the detector [25]. To fulfil this requirement, the beam pipe aperture design in the detector region needs to be revisited. The goal can be achieved by increasing the apertures of the incoming beamline in the BeamCal region. The apertures should be increased to match the QD0 aperture at each energy stage. Direct photons have a very low divergence; thus, this extension is sufficient to ensure the safety of the kicker system, and minimises photon scattering in the BeamCal region.

The updated beam pipe design in the detector region for the 380 GeV energy stage is summarised in Table 2, and in Table 3 for 3 TeV, using the CLICdet detector model design as the starting point [11]. The inner radius between the longitudinal position of 2700 mm and 3500 mm in the incoming beamline is extended from 2.7 mm to 17.5 mm at 380 GeV, and from 2.7 mm to 7.6 mm in the 3 TeV detector model. The beam pipe thickness is kept at 1 mm.

These detector models with updated apertures are used in the full-detector simulations performed to evaluate the effect of SR photons on occupancy levels, rather than those described in Ref. [11].

4.2. Photon distributions at the QD0 exit

The photons propagated through the FFS geometry by Synrad+ are stored, in the general case, at the exit of the final focus quadrupole magnet, QD0. The transverse and angular distributions of the SR photons at this position determine the radiation impact on the CLIC detector. The parameter used to quantify the effect is the polar angle, θ_{QD0}, calculated relative to a reference point in the centre of the beampipe at the QD0 exit, 6 m upstream from the IP.

Polar angles θ_{QD0} are calculated for each SR photon to estimate the flux and energy that can be deposited in the detector. Polar angle distributions of the SR photons are shown in Fig. 10. The distributions are split into two parts depending on the origin of photons. Direct photons, coming from the last few bending magnets and the final focus quadrupoles are emitted with small polar angles and occupy the left-hand side of the figure. The flux of direct photons dominates the distribution, however they do not contribute to the total energy that can be deposited in the detector. The reflected photons have significantly larger polar angles, spanning from 1 mrad to almost $\frac{\pi}{2}$. Due to larger apertures, the reflected photons are more numerous at 380 GeV in comparison with the 3 TeV energy stage, by a factor of about ten when using the same material and roughness.

Photons with polar angles larger than 3.3 mrad, as shown in Fig. 10, where the reference point is located in the centre of the beam pipe at the QD0 exit, 6 m upstream from the IP, are capable of interacting with at least the material of the BeamCal located on the opposite side (later referred to as 'far-side') of the detector. Photons with such polar angles are recognised as 'visible' in the detector, and the total energy they carry in each studied case is summarised in Table 4.

The polar angle distributions of photons coming from a BDS with fully absorbing vacuum chamber walls at both energy stages are constrained to the small polar angles, as only the direct photons traverse the QD0 aperture. Therefore, in the case when the fully absorbing walls are used in the FFS, the SR photons do not interact with the material

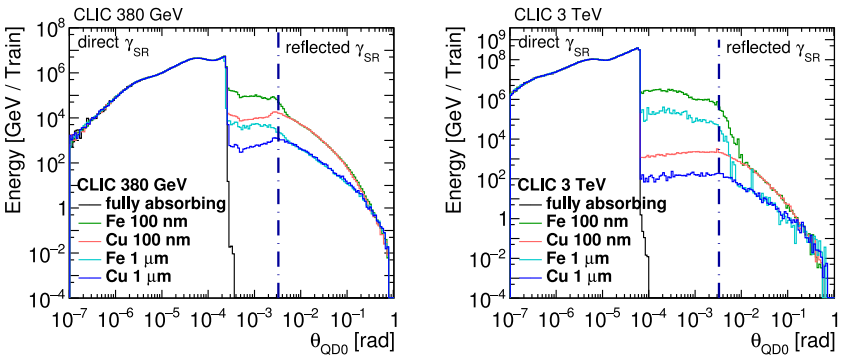

Fig. 11. The angular distribution of the energy carried by synchrotron radiation photons at the QD0 exit at 380 GeV (a) and 3 TeV (b) with copper and iron vacuum chamber walls with 1 μm and 100 nm average surface roughness simulated with Synrad+. θ_{QD0} signifies the polar angle where the reference point is located in the centre of the beampipe at the QD0 exit, 6 m upstream from the IP. The marked BeamCal aperture refers to the outgoing beam pipe radius in the BeamCal located on the opposite side of the detector.

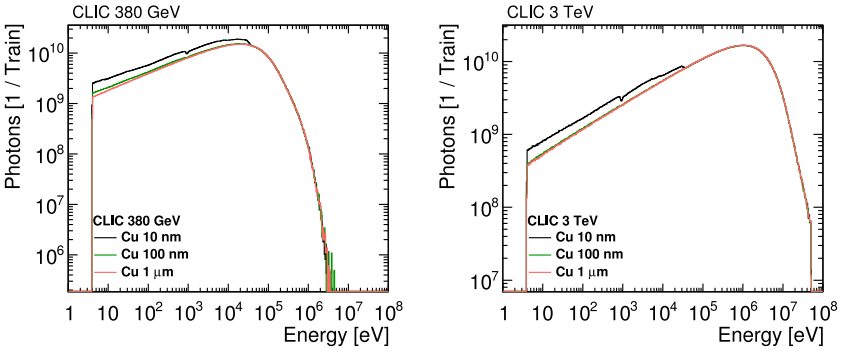

Fig. 12. Energy distributions of synchrotron radiation photons at the QD0 exit at 380 GeV (a) and 3 TeV (b), using copper vacuum chamber walls with 1 μm, 100 nm, and 10 nm surface roughness simulated with Synrad+.

of the detector, fulfilling the detector safety requirement. This result is consistent with PLACET simulations, where photons produced in the final doublet and the last few bending magnets cannot interact with the sensitive material of the detector. The absence of the SR photons in the acceptance of the detector is the desired experimental condition. It ensures there are no accidental hits and unwanted energy depositions in the tracking detector, also in the form of additional heat.

The application of realistic reflectivities of copper and iron leads to a substantial amount of visible energy that can be deposited in the detector. The photon distributions strongly depend on the reflectivity of the material and its average roughness. A change of R_a by a factor of ten, from 1 μm to 100 nm, increases the number of reflected photons that can hit the sensitive material of the detector by a factor of fifteen at 380 GeV and twenty-five at 3 TeV. The number of photons quickly decreases with increasing polar angle in all studied cases.

The total visible energy of the SR photons is of a significant magnitude, even where a rough copper surface with R_a of 1 μm is used, as shown in Table 4. The visible energy surpasses the nominal collision energy at 380 GeV, and is comparable with the collision energy at 3 TeV. The amount of energy is higher at 380 GeV than at 3 TeV when copper is used as the vacuum chamber material, but the opposite is true when the vacuum chamber is made of iron. The difference in the number of reflected photons between copper and iron vacuum chamber, as shown in Fig. 10, is not as large as the difference in the visible energy. The angular distribution of the energy carried by photons, which provides an explanation to this observation, is shown in Fig. 11. The difference in the distributions is the result of a harder energy spectrum at the higher energy stage, that leads to a lower probability of reflections. The other factor is the higher reflectivity of iron in comparison with copper. The use of iron for the vacuum chamber wall results in significantly more energy deposited in the detector region than when copper of the same roughness is used, and thus the use of iron without copper coating should be avoided.

The energy distributions of the SR photons traversing the QD0 aperture, similarly to the polar angle distributions, have contributions from both direct photons produced in the final doublet quadrupoles and the last few bending magnets, as well as photons that underwent reflections. Direct photons dominate over the reflected ones, and define the shape of the distributions, as shown in Fig. 12. Direct photons are all photons with energy above 30 keV, and constitute most of the photons.

The contribution from the reflected photons enhances the number of low energy photons when the average roughness is below 100 nm, as can be seen in Fig. 12. However, the impact of the enhancement on the average photon energy is limited and is not larger than 8% of the relative value between material choices and roughnesses. The average photon energy is in the 100 keV range at 380 GeV, and is a factor forty larger at 3 TeV, reaching the MeV-range. The critical energy in the weak bending magnets is fifty-six times larger at 3 TeV than at 380 GeV, even though the magnets have a factor ten lower bending angle. The difference in the average photon energy is smaller than the difference in the critical energy in the bending magnets. The emission of lower energy photons in the bending magnets at 380 GeV is compensated by the emission of higher energy photons in the quadrupole magnets at the lower energy stage, caused by larger beam divergence and size than at 3 TeV.

The average SR photon energies at the exit of the QD0 magnet are smaller than the average energy of all the photons emitted in the BDS at each energy stage. This is due to the lower intensity and less energetic emissions in the weak bending magnets and quadrupole in the final metres of the FFS than in the stronger bending magnets present in the collimation region of the BDS. The distribution at the QD0 exit lacks the higher energy photons produced upstream because photons with energies above 30 keV have negligible reflectivity and therefore do not reach the detector region.

The energy distributions of the photons with polar angle above 3.3 mrad are shown in Fig. 13. The shape of the distributions is sensitive

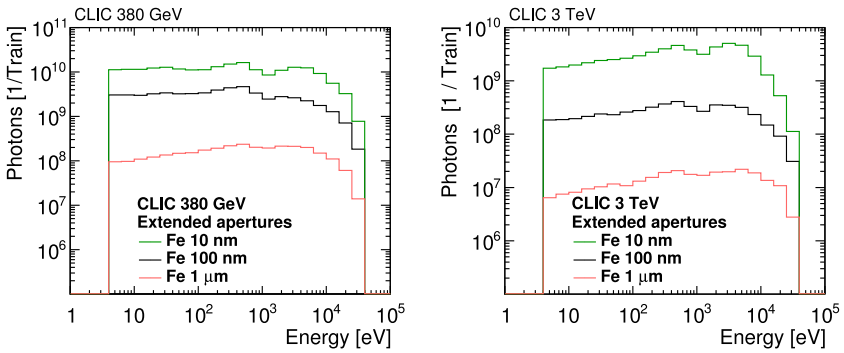

Fig. 13. Energy distributions of synchrotron radiation photons with $\theta_{QD0} > 3.3$ mrad at the QD0 exit at 380 GeV (a) and 3 TeV (b), using copper vacuum chamber walls with 1 μm, 100 nm and 10 nm surface roughness simulated with Synrad+.

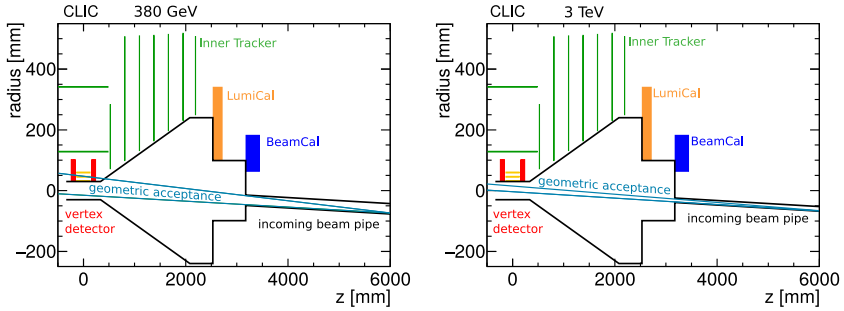

Fig. 14. Geometric acceptance of synchrotron radiation photons taking into account the incoming beam pipe geometry at 380 GeV (a) and 3 TeV (b).

to the used material and average roughness. The higher reflectivity cases have a larger dip in the 1–2 keV energy range that splits the distribution into two parts. The dip is caused by a minimum of reflectivity in this energy range. An increase in reflectivity changes in particular the low energy part of the distribution, as these photons have the highest probability of reflection while the higher energy range is fully determined by the direct photons emitted in the weak bending magnets and final focus quadrupoles. Therefore, the average energy of photons decreases with increasing reflectivity. The average energy varies from 1.8 keV to 2.3 keV at 380 GeV and from 2.0 keV to 3.2 keV at 3 TeV. Although the average energies of emitted photons differ significantly between the energy stages, by a factor of forty, the average energy of photons that can impact the detector are similar.

The low energy part, with photons below 1 keV does not constitute a risk of increasing the occupancy level in the detector, as the energy deposits are below the energy threshold for all of the detectors. These photons can lead mostly to the heating of the beam pipe in the detector region, and the detectors located closest to the IP region. However, the low energy photons can also induce radiation damage after an extended period of exposure. The total power carried by the SR photons passing through the QD0 aperture is equal to 0.5 W at 380 GeV and 25 W at 3 TeV. The photons that are in the acceptance of the detector, further called 'visible photons', carry only a small fraction of the photon beam power, 2.8 mW at 380 GeV and 0.9 W at 3 TeV, but is still substantial enough to cause damage, especially at the higher energy stage. Therefore, the radiation damage from the unmitigated SR in the detector region may be a concern, and the energy depositions in the tracking detector will have to be simulated in GEANT4 .

In summary, the desired experimental conditions without the unwanted SR photons in the acceptance of the detector are provided at both energy stages by using, purely hypothetical, fully absorbing vacuum chamber walls. Realistic material reflectivities lead to substantial amounts of energy that can be deposited in the detector. The use of iron as the material for the beam pipe is not advised, as for the same aperture and average roughness it leads to a larger number of photons that can impact the detector negatively in comparison with copper. The energy that is visible in the detector scales strongly with the average material roughness used in the FFS. Based on realistic material reflection tables, the best experimental conditions are provided by a copper surface with an average roughness around 1 μm.

4.2.1. Geometric acceptance of the photons

Direct SR photons can interact with the sensitive material of the detector if their polar angles are larger than 3.3 mrad. However, for direct photons the polar angle also needs to be lower than the limit imposed by the beam pipe aperture of the incoming beamline, so the SR photons do not interact with the beam pipe multiple times. Otherwise, only indirect interaction is possible, where a photon needs to scatter to interact with the sensitive material of the detector. The borders of the geometric acceptance limited by the aperture in the BeamCal region is shown in Fig. 14.

The synchrotron radiation photons that are travelling through the QD0 aperture can interact directly with the Vertex detector barrel and disks at 380 GeV. The rest of the tracking detector is outside of the geometric acceptance, thus is expected to receive a significantly smaller number of hits than the Vertex detector. At 3 TeV, even the Vertex detector is outside the geometric acceptance, as shown in Fig. 14(b). Therefore, at 3 TeV, the photons can only interact with the sensitive material of the trackers indirectly, after scattering in the beam pipe in the BeamCal region.

Photons with considerable angles $\theta_{QD0} \approx \frac{\pi}{2}$ can interact with the material of the yoke endcap and the HCal endcap. The high energy threshold of 300 keV for detection in the HCal endcap cells surpasses the maximum energy of photons in the detector acceptance by a factor of ten. Multiple simultaneous hits from the SR photons could leave energy depositions above the threshold. However, this is not observed in the full detector simulations.

The MuonID system could be impacted if photons penetrate the beam pipe and find themselves between the iron yoke plates because the energy threshold of the gaseous sensitive elements is only 300 eV. Similarly to the HCal endcap, no energy depositions above threshold are observed in full detector simulations.

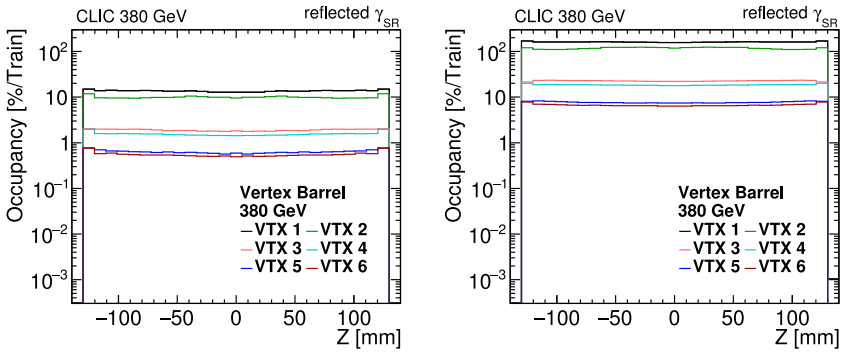

Fig. 15. Distribution of the occupancies per bunch train in the Vertex barrel at 380 GeV coming from synchrotron radiation photons reflected in the FFS, assuming average roughness of the copper vacuum chamber wall of 1 μm (a) and 100 nm (b).

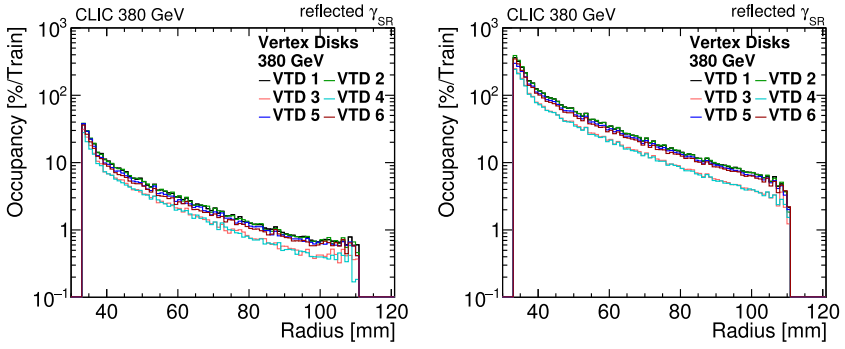

Fig. 16. Distribution of the occupancies per bunch train in the Vertex disks at 380 GeV coming from synchrotron radiation photons reflected in the FFS, assuming average roughness of the copper vacuum chamber wall of 1 μm (a) and 100 nm (b).

The ECal endcap should not be affected negatively by SR because the 40 keV energy threshold of the silicon sensors is above the maximal energy of the photons. In addition, the ECal endcap is shielded from the SR photons entering the detector by the HCal endcap . The SR photons cannot point directly at the far-side ECal endcap, as the required polar angle is at least 31 mrad, while the limitation imposed by the BeamCal aperture is below this number at both energy stages.

The ECal and HCal barrels and the MuonID barrel are also safe from the SR due to their distant position from the central beam pipe and the low probability of photons scattering in the centre of the detector to gain the necessary polar angle to point towards these subdetectors. The scattered photons would need to traverse all of the material between the IP region and the detector, and leave energy depositions over threshold in the sensitive elements of these detectors, which is highly unlikely.

The SR photons are also unlikely to impact the forward calorimeters, even on the near-side of the detector. The BeamCal shadows the LumiCal, and therefore the latter remains safe from the SR. The SR photons would need to penetrate the beam pipe at low grazing angles and then traverse the tungsten absorber plates to reach the sensitive material of the BeamCal.

The only detectors that can be strongly impacted by the SR photons are the Vertex and Inner Tracker detectors, due to their positions close to the beam pipe and the relatively low energy thresholds in the keV range.

The larger beam pipe aperture in the 380 GeV detector model increases the likelihood relative to the 3 TeV design that the Vertex and Tracker receive significant energy depositions. At 3 TeV, photons need to scatter in the beam pipe material within the detector region to increase their polar angle such that hits in the tracking detectors can be produced. Therefore, the hit rates for the same total energy of photons with polar angles above 3.3 mrad should be significantly lower at 3 TeV than at 380 GeV. The larger beam pipe aperture in the 380 GeV detector model increases the proportion of the visible energy that can interact with the sensitive elements of the detector than at 3 TeV.

4.3. Hit densities and occupancies in tracking detectors

The occupancies in the tracking detectors are calculated using Eq. (1), assuming a cluster size of five in the Vertex detector and of two in the Tracker, and including a safety factor of two. In the full detector simulations, SR photons originating from the BDS are modelled using copper vacuum chamber walls and under two roughness scenarios, 1 μm and 100 nm are used.

The SR photons used for the hit densities calculations are obtained from Synrad+ simulations with an electron beam. The detector is impacted by SR photons coming also from the positron beam. To take this into account and to remove the asymmetry from using a single incoming beam direction, the hit distribution determined using GEANT4 simulations is added with itself, reflected in the transverse XY-plane.

4.3.1. 380 GeV

The occupancies from reflected SR photons in the Vertex barrel for copper with (R_a) values of 1 μm and 100 nm are shown in Fig. 15(a) and Fig. 15(b), respectively. The factor of ten decrease in roughness leads to a factor of ten increase in the number of hits observed in the Vertex detector. The occupancy surpasses 100% in the 100 nm roughness case. In both cases, the occupancy is significantly above the 3% acceptable limit [29] in the first double layer of the Vertex detector barrel. The hit density severely impacts the detector performance when R_a is 1 μm, and none of the intended physics analyses will be possible when R_a is at or below 100 nm.

The occupancy levels of the Vertex disks are shown in Fig. 16. At the lowest radii, the hit densities are even larger than in the Vertex barrel, due to the lower polar angles of the disks located on the opposite side of the IP. The occupancy reaches 30% in the case when R_a is 1 μm copper is used, and is more than a factor ten larger at the lowest radii when a less rough vacuum chamber surface is used in the FFS.

The disks located in the middle of the forward region of the Vertex detector, namely disks VTD 3 and VTD 4, have consistently lower hit

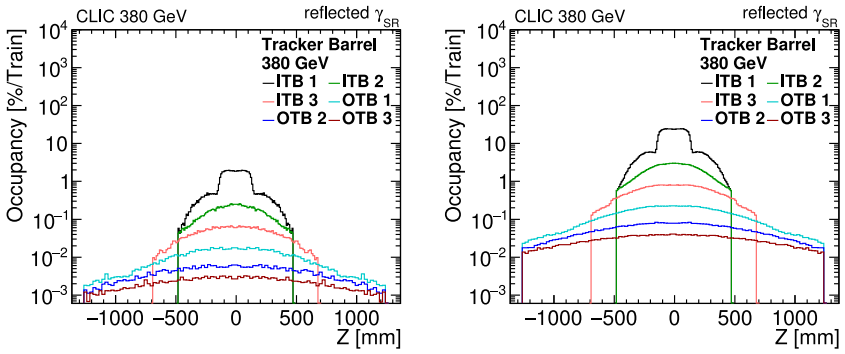

Fig. 17. Distribution of the occupancies per bunch train in the Tracker barrel at 380 GeV coming from synchrotron radiation photons reflected in the FFS, assuming average roughness of the copper vacuum chamber wall of 1 μm (a) and 100 nm (b).

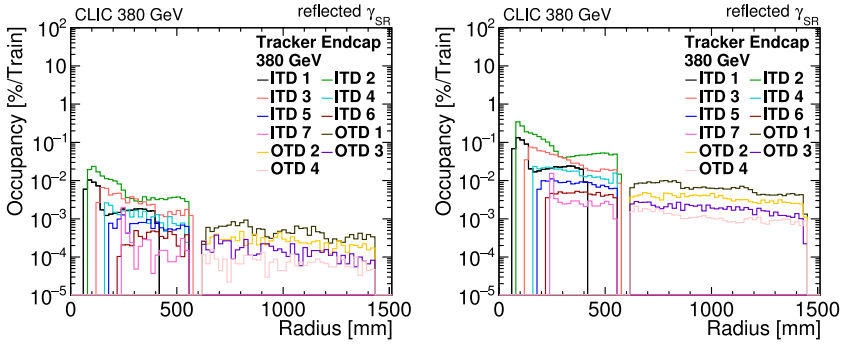

Fig. 18. Distribution of the occupancies per bunch train in the Tracker disks at 380 GeV coming from synchrotron radiation photons reflected in the FFS, assuming average roughness of the copper vacuum chamber wall of 1 μm (a) and 100 nm (b).

rates than either disks VTD 1 and 2 or VTD 5 and 6. The lower hit rates can be explained by disks located on either side shielding those the disks in the middle.

The occupancies are much lower in the Inner and Outer Tracker barrel than in the Vertex detector. The most impacted is the first Inner Tracker layer, as shown in Fig. 17, where the hits caused by the SR photons have a 'top hat'-like distribution. Such a distribution of hit density is a result of the transition between being impacted by the 'direct' photons that travelled in a straight line from the QD0 exit, and the hits that are from photons that scattered while traversing material of the beam pipe or inner detectors, including the support structures.

The occupancy distributions of the Tracker barrel are shown in Fig. 17. The maximal occupancy is close to the 3% limit for the first layer of the Inner Tracker when 1 μm roughness is used, and safely below the limit for layers located further away from the beam pipe. When higher reflectivity copper is used, the photon impact on the Tracker is more severe, and only the last layer of the Inner Tracker is below the occupancy limit.

The impact of the SR photons in the Tracker disks is much lower than in the other tracking subdetectors. The occupancy levels are shown in Fig. 18. The low hit rates are due to the position of the detector behind the conical beam pipe with 4 mm thick steel walls, which provide shielding. With the exception of the lowest radius of the first disk, the disks cannot be hit by 'direct' photons without additional scattering, as the required polar angle is larger than the limit imposed on the photons in the BeamCal region.

The most impacted elements of the Tracker are the two first disks of the Inner Tracker, and especially their lowest radii, located closest to the beam pipe. The occupancies, reach up to 0.4% for the 100 nm R_a beam pipe option and are below 0.03% when the beam pipe in the FFS is rougher.

Only a fraction of the total visible energy presented in Table 4, is deposited in the tracking detectors. The total energy deposited per bunch train is equal to 1% of the visible energy when the 1 μm R_a copper is used and reaches 7% in the 100 nm roughness case.

4.3.2. 3 TeV

The SR photon distributions coming from the 3 TeV FFS Synrad+ simulations and embedded in the CLIC detector model with optimised beam pipe apertures result in zero hits recorded in the sensitive material of the detector. The photons simulated in GEANT4 are entirely absorbed in the beam pipe walls before they reach the material of the Vertex and Tracker.

The lower hit density at 3 TeV than at 380 GeV is expected due to the lower visible energy per bunch train (see Table 4), and the smaller geometric acceptance for the SR photons, that does not include the sensitive material of the Vertex detector (see Fig. 14(b)). However, a complete lack of energy depositions is not expected. Taking into account the limitations of the GEANT4 description of the low-energy photons, namely an absence of reflections phenomena for the *gamma* photon particle type, a change in the simulation conditions needs to be considered.

A possible approach is to track the SR photons further downstream in Synrad+, up to the end of the BeamCal at 3170 mm from the IP. This approach changes the total energy of photons in the acceptance of the detector from 0.9 TeV to 0.4 TeV per bunch train when 1 μm average roughness copper is used, and from 11 TeV to 5.1 TeV when R_a is 100 nm. The result is about a 50% reduction in the energy that can be deposited in the sensitive material of the Vertex and Tracker detectors.

The occupancies from the reflected SR photons in the Vertex barrel are shown in Figs. 19(a) and 19(b), for R_a values of 1 μm and 100 nm, respectively. Similarly to the 380 GeV results, a factor of ten decrease in roughness leads to a proportional increase in the number of hits observed in the Vertex detector. The occupancy levels reach 10% in the 100 nm roughness case, as shown in Fig. 19. In the case of copper surface with R_a of 1 μm, the occupancy in the Vertex barrel reaches 1% for the first double layer and is below that value for layers located at larger radii.

The occupancy distributions of the Vertex disks are shown in Fig. 20. At the lowest radii, the occupancies are significantly larger than in the

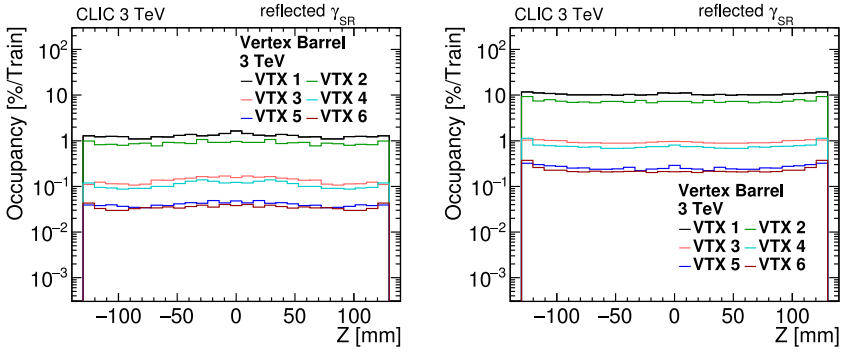

Fig. 19. Distribution of the occupancies per bunch train in the Vertex barrel at 3 TeV coming from synchrotron radiation photons reflected in the FFS, assuming average roughness of the copper vacuum chamber wall of 1 μm (a) and 100 nm (b).

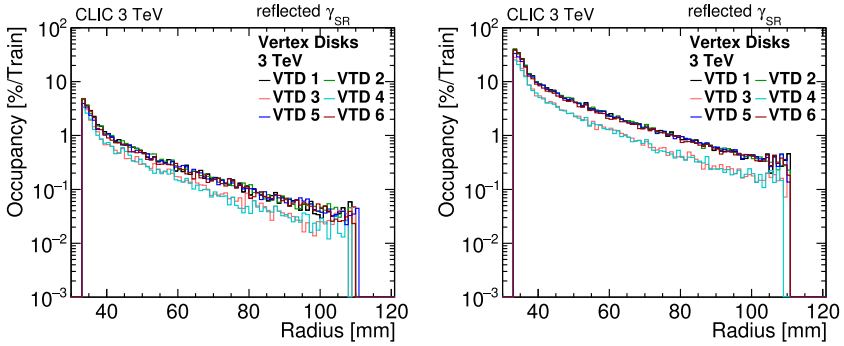

Fig. 20. Distribution of the occupancies per bunch train in the Vertex disks at 3 TeV coming from synchrotron radiation photons reflected in the FFS, assuming average roughness of the copper vacuum chamber wall of 1 μm (a) and 100 nm (b).

Vertex barrel, due to the smaller polar angles of the disks located on the opposite side of the IP. The occupancy, shown in Fig. 20, reaches 5% in the 1 μm copper case and is about 40% at the lowest radii when a less rough vacuum chamber surface is used in the FFS.

As observed for the 380 GeV energy stage, the disks located in the middle of the forward Vertex detector, namely disks VTD 3 and VTD 4, have consistently lower hit rates than either disks VTD 1 and 2 or VTD 5 and 6. The explanation is the same as for the 380 GeV results.

The hit densities and occupancies are much lower in the Inner and Outer Tracker barrel than in the Vertex detector, especially for layers located further away from the beam pipe. The most impacted is the first Inner Tracker layer, as shown in Fig. 21, where the hits caused by the SR photons again have a 'top hat'-like distribution. The maximal occupancy is close to 1% for the first layer of the Inner Tracker when 100 nm roughness is used, well below the 3% acceptable occupancy. The layers located further away from the beam pipe are not significantly impacted by the SR photons, and have occupancy levels below 0.1% . When rougher copper surface is used, the photon impact on the Tracker is even smaller, and all of the Inner Tracker layers are below the 0.1% occupancy level.

Similarly to the 380 GeV energy stage results, the impact of the SR photons in the Tracker disks is much lower than in the other tracking subdetectors. The occupancies are shown in Fig. 22. The rates are significantly below the 380 GeV levels, by a factor of approximately 30. This is a more substantial difference than can be expected from a simple comparison of the visible energy in Table 4, where the visible energy of the SR photons at 3 TeV is smaller by only a factor of 7 than at 380 GeV. The observed discrepancy can be attributed to the difference in geometrical acceptance between the energy stages. The occupancies are negligible (below the 0.01% level) for the smooth beam pipe option and a factor of ten lower when the beam pipe in the FFS has R_a of 1 μm.

5. Mitigation methods

The impact of the SR photons on the detector is severe at 380 GeV. The observed occupancies create extremely challenging experimental conditions for the Vertex and Inner Tracker detectors unusable when the average surface roughness of copper is below 1 μm. The situation is different at 3 TeV, where the occupancy levels are significantly smaller, due to the geometry of the interaction region that makes it unlikely for the SR photons to hit sensitive elements linked with the small apertures in the BeamCal region, which limit the maximal polar angle θ_{QD0} of the photons. However, the visible energy of the SR photons is still substantial and the occupancy levels for R_a of 100 nm are above the 3% limit at 3 TeV. Therefore, a mitigation method should be put in place for maximal safety of the detector at both energy stages.

The desired experimental conditions are to have no SR photons in the detector acceptance. In the case when the SR photons cannot be excluded entirely, the mitigation should aim to minimise the energy that can be deposited in the detector and the occupancy levels. Such conditions are ensured in the ideal case where the vacuum chamber is completely non-reflective. Therefore, a mitigation method providing similar conditions to ensure the detector safety and performance has to be developed.

There are a few ways in which the high fluxes of SR photons within the detector acceptance can be addressed. The first is to reduce the reflectivity of the vacuum chamber by increasing the average roughness of the surface. A value of R_a equal to 7 μm for the 380 GeV BDS is sufficient to minimise the impact of the SR photons in the detector region. The average visible energy per bunch train is not reduced to zero; however, according to full detector simulations in GEANT4 photons do not leave significant energy deposits in the tracking detectors, and the maximal occupancies are reduced to below 1% level in the Vertex detector.

The required increase of surface roughness can be achieved, for example, through laser ablation. This treatment of the surface is a stable

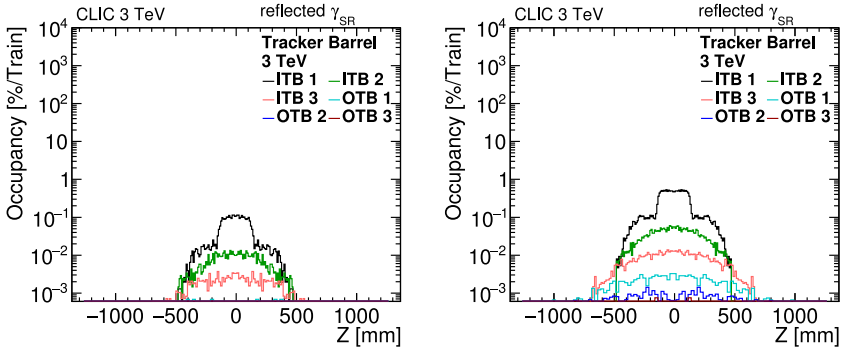

Fig. 21. Distribution of the occupancies per bunch train in the Tracker barrel at 3 TeV coming from synchrotron radiation photons reflected in the FFS, assuming average roughness of the copper vacuum chamber wall of 1 μm (a) and 100 nm (b).

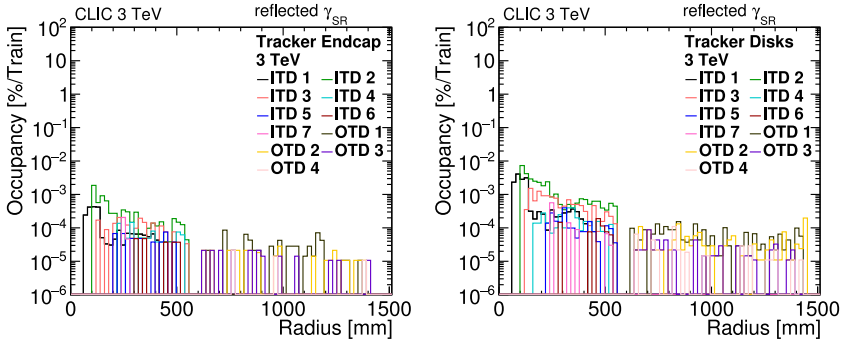

Fig. 22. Distribution of the occupancies per bunch train in the Tracker disks at 3 TeV coming from synchrotron radiation photons reflected in the FFS, assuming average roughness of the copper vacuum chamber wall of 1 μm (a) and 100 nm (b).

and inexpensive method of increasing the average roughness [39]. The surface treated with a laser has the additional advantage of lowering the yield of secondary electrons emitted as a result of interactions with SR photons, thus lowering the outgassing rate and suppressing the creation of an electron cloud [39,40].

The main disadvantage of the approach where the surface roughness is considered, is the consequent increase of the impedance [41]. The beams would be subject to stronger wakefield effects, and the beam energy spread and transverse beam sizes would increase that leads to a decrease in the performance of the accelerator. To mitigate wakefields, an increase in apertures would be desirable. However, a general increase of circular vacuum chamber radii in the FFS, in turn, increases the photon flux in the detector region and counteracts the benefits from this mitigation approach.

A similar method aiming to reduce the reflectivity is based on installing a saw-tooth shape on the inner wall of the vacuum chamber on the side where reflections of the synchrotron radiation take place. An example of such saw-tooth, based on the experiences of the LHC vacuum chamber design [28] is shown in Fig. 23(b). The layout of the circular vacuum chamber with a saw-tooth shape installed, as simulated with Synrad+, is shown in Fig. 23(a). A saw-tooth layout of similar design is also foreseen for the FCC-hh [14].

The saw-tooth shape is one of the available "materials" in the Synrad+ libraries, and its impact on the SR photons flux in the detector region can be studied using the existing tools. The simulations suggest that it is sufficient to install the saw-tooth in the final 30 m of the FFS, from the last bending magnet to the QD0 exit, to reduce the reflectivity to the point, where the SR photons are not visible in the detector acceptance. The result at both energy stages achieves the same experimental conditions as if the vacuum chamber was fully absorbing along the entire FFS. A safety margin can be ensured by extending the region where the saw-tooth is installed by an additional 100 m upstream, and downstream to the kicker system.

The disadvantage of installing the saw-tooth is the same as in the roughness increase approach: an increase in impedance, and consequently in wakefields experienced by the beams. The impact of the increased impedance can be mitigated in both cases by extruding the circular vacuum chamber to create a 'winglet'-shaped aperture. In one of the extruded arms, sufficiently distant from the beam pipe axis, the saw-tooth or a rough surface can be placed to limit the negative impact on the beam stability. Such a design, based on the idea developed for the FCC-ee vacuum chamber [36] is shown in Fig. 24. The winglet could be cooled or shielded on the side irradiated by the SR photons if it were found to be necessary.

An alternative method to mitigate the large photon fluxes is to install SR masks in the detector region, similar to the approach used in LEP2 [16]. A collimator or a synchrotron radiation mask needs to be installed upstream of the BeamCal and the kicker on the incoming beamline to protect these elements from the SR irradiation. Such a mask, made of lead or tungsten, can be implemented in the GEANT4 detector model as a reduction in vacuum chamber aperture. Given the constraints on available space in the forward region, tungsten with its shorter radiation length is the preferred material.

Taking into account only the photons with $\theta_{QD0} > 3.3$ mrad which are in the acceptance of the detector, it is sufficient to reduce the aperture upstream from the BeamCal down to 6 mm. Photons that cause high occupancy levels have energy below 30 keV, where electromagnetic cascades or neutron photo-emissions do not take place. Therefore, these

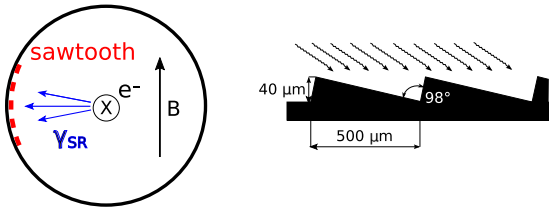

Fig. 23. Z-axis projection of the saw-tooth with design details (b) and saw-tooth layout inside the beam pipe as used in the Synrad+ model of the CLIC FFS (a) [38].

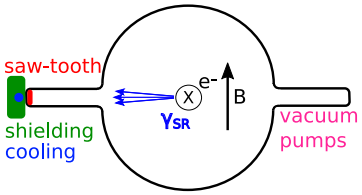

Fig. 24. Winglet aperture shape based on the vacuum system under development for FCC-ee [36] with saw-tooth shape located further away from the beam pipe centre axis and schematic diagram of possible shielding.

photons do not cause significant scattering in the forward region of the detector when they interact with the beam pipe material. However, the SR mask necessarily needs to absorb all photons that are at a larger offset than 6 mm. The photons with energies higher than 30 keV and at offsets larger than 6 mm travel through the detector region without interacting with any material of CLICdet. When the SR mask is implemented, these higher energy photons will cause scattering in the forward detector region, which makes the design of such a mask more challenging. The number of photons further away from the beam pipe axis increases with increasing reflectivity, as was shown in Fig. 8, therefore more energy needs to be absorbed in the high-reflectivity cases.

A combination of methods can also be envisioned. In this approach, the winglet shape is used in the final metres of the FFS, and in the detector region, the arm that hosts the saw-tooth shape is fully filled with a short radiation length material instead. The photons in the winglet would then be absorbed, and the decrease of aperture would not impact the beam stability.

In summary, two main approaches to the mitigation of large SR photon fluxes found in the detector acceptance can be pursued. The most promising from the safety perspective is to remove the photons before they can reach the detector. The number of the SR photons that can interact with the sensitive material of the detector can be limited by reducing the reflectivity of the vacuum chamber surface, either by modifying the surface or installing the saw-tooth shape. The reflectivity reduction should be placed in the extruded arms of the 'winglet' shape, located further away from the centre of the beam pipe to reduce wakefields. The advantage of this approach is that it is independent of the GEANT4 predictions and its modelling of very low-energy electromagnetic processes. It does depend on the accuracy of the Synrad+ reflectivity model; however, this has been validated [27].

6. Summary and conclusions

The impact of SR was found to be a significant issue at CLIC, at both energy stages studied, especially when the reflections of the radiation are taken into account.

In the hypothetical case of non-reflective surfaces in the CLIC FFS, no SR photons end up in the acceptance of the detector. However, the materials that can be used for the vacuum chamber walls have non-negligible reflection probability up to a photon energy of about 30 keV. This leads to a large number of photons that travel significantly further along the accelerator and can interact with the sensitive material of the detector.

The heating caused by the SR photons interacting with the beam pipe material does not cause a significant increase of the temperature at 380 GeV while at 3 TeV, the heating is substantial and needs to be addressed by a dedicated active cooling system, especially in the collimation region of the Beam Delivery System.

The hit densities and related occupancy levels in the tracking detectors arising from SR photons are high at both energy stages, especially so at 380 GeV. There, the detector is strongly influenced by SR photons even when the beam pipe surface has an average roughness of 1 μm. An increase of reflectivity in the FFS leads to more numerous photons in the acceptance of the detector and higher hit rates, proportional to the increase in the visible energy.

The occupancy in the Vertex detector at 380 GeV is significantly above the 3% limit, even when the copper vacuum chamber surface has an average roughness of 1 μm. Using a less rough surface with 100 nm average roughness leads to occupancies reaching 100% in the Vertex barrel and endcaps. At 3 TeV, the occupancies reach 10% for the first double layer when the 100 nm roughness is used, and is below 1% when the roughness is 1 μm. For both energy stages, the hit rates are significantly lower in the Tracker barrel and endcaps. The thick walls of the conical beam pipe shield the endcap disks. Most of the Tracker barrel layers are not directly reachable from the QD0 exit and every registered hit is caused by a photon that had to scatter while traversing the material of the detector. This significantly lowers the probability of receiving a hit.

The high occupancies in the Vertex detector would significantly deteriorate the performance of the Tracker. The non-reflective vacuum chamber surface in the FFS provides the desired experimental conditions, thus approaches based on reducing the reflectivity offer mitigation of the high photon fluxes. A reduction of reflectivity can be achieved by increasing the roughness of the surface or by the implementation of a saw-tooth absorber similar to the LHC design. It is sufficient to cover the final 30 m of the FFS to achieve the same outcome as if the vacuum chamber walls were wholly absorbing along the entire FFS. However, the roughness increase or the installation of a saw-tooth absorber increases the impedance and leads to stronger wakefields that decrease the quality of the beam. To counteract the increase of wakefields, the saw-tooth can be placed in an extruded arm of the circular beam pipe, creating a 'winglet' shape that is foreseen to be used in the vacuum system of the FCC-ee. The result of the implementation of this approach is the absence of the SR photons in the detector acceptance and the optimal experimental conditions. Additional simulations in GEANT4 or FLUKA of the saw-tooth element should be pursued to optimise the height and thickness of the teeth for the CLIC synchrotron radiation energy spectrum.

The results of the simulations of the synchrotron radiation in the FFS can be used as input for the study of the active cooling of the beam pipe. The active cooling should be studied further for the 3 TeV energy stage.

Declaration of competing interest

The authors declare that they have no known competing financial interests or personal relationships that could have appeared to influence the work reported in this paper.

Acknowledgements

Special thanks to Marton Ady and Roberto Kersevan for valuable discussions and support.

This research was done using resources provided by the Open Science Grid, which is supported by the National Science Foundation and the U.S. Department of Energy's Office of Science. This work benefited from services provided by the ILC Virtual Organisation, supported by the national resource providers of the EGI Federation.

References

[1] J.-M. Chaize, et al., The ESRF's extremely brilliant source - a 4th generation light source, in: Proceedings, 16th International Conference on Accelerator and Large Experimental Physics Control Systems, ICALEPCS 2017, Barcelona, Spain, October 8–13, 2017, http://dx.doi.org/10.18429/JACoW-ICALEPCS2017-FRAPL07.

[2] C. Wyss, LEP Design Report, V.3: LEP2, Vol. 1–2, CERN, Geneva, 1996, URL http://cds.cern.ch/record/314187.

[3] M. Benedikt, A. Blondel, O. Brunner, M. Capeans Garrido, F. Cerutti, J. Gutleber, P. Janot, J.M. Jimenez, V. Mertens, A. Milanese, K. Oide, J.A. Osborne, T. Otto, Y. Papaphilippou, J. Poole, L.J. Tavian, F. Zimmermann, Future Circular Collider, CERN-ACC-2018-0057, CERN, Geneva, 2018, URL http://cds.cern.ch/record/2651299, Dec.

[4] CEPC Study Group Collaboration, CEPC Conceptual Design Report: Vol. 1 - Accelerator, 2018, arXiv:1809.00285.

[5] R. Jacobsen, et al., Detector background conditions at linear colliders, in: Instrumentation for Colliding Beam Physics. Proceedings, 5th International Conference, Novosibirsk, USSR, March 15–21, 1990, 1990, pp. 0455–0461, URL http://www-public.slac.stanford.edu/sciDoc/docMeta.aspx?slacPubNumber=SLAC-PUB-5205.

[6] T. Behnke, J.E. Brau, B. Foster, J. Fuster, M. Harrison, J.M. Paterson, M. Peskin, M. Stanitzki, N. Walker, H. Yamamoto, The International Linear Collider Technical Design Report - Vol. 1: Executive Summary, 2013, arXiv:1306.6327.

[7] P.N. Burrows, et al., CLICdp, CLIC Collaboration, The Compact Linear Collider (CLIC) - 2018 Summary Report, CERN Yellow Report, 2018, http://dx.doi.org/10.23731/CYRM-2018-002, arXiv:1812.06018.

[8] M. Aicheler, P.N. Burrows, N. Catalan Lasheras, R. Corsini, M. Draper, J. Osborne, D. Schulte, S. Stapnes, M.J. Stuart, CLIC accelerator Collaboration, The Compact Linear Collider (CLIC) - Project Implementation Plan, CERN Yellow Report, 2019, http://dx.doi.org/10.23731/CYRM-2018-004, arXiv:1903.08655.

[9] D. Dannheim, et al., Detector Technologies for CLIC, CERN Yellow Report, 2019, http://dx.doi.org/10.23731/CYRM-2019-001, arXiv:1905.02520.

[10] B.L. Henke, E.M. Gullikson, J.C. Davis, X-ray interactions: Photoabsorption, scattering, transmission, and reflection at E = 50-30,000 eV, Z = 1-92, Atom. Data Nucl. Data Tabl. 54 (2) (1993) 181–342, http://dx.doi.org/10.1006/adnd.1993.1013.

[11] N. Alipour Tehrani, et al., CLICdet: The Post-CDR CLIC Detector Model, CLICdp-Note-2017-001, 2017, URL https://cds.cern.ch/record/2254048.

[12] M. Boscolo, H. Burkhardt, M. Sullivan, Machine detector interface studies: Layout and synchrotron radiation estimate in the future circular collider interaction region, Phys. Rev. Accel. Beams 20 (1) (2017) 011008, http://dx.doi.org/10.1103/PhysRevAccelBeams.20.011008.

[13] F. Collamati, M. Boscolo, H. Burkhardt, R. Kersevan, Synchrotron radiation backgrounds for the FCC-hh experiments, in: Proceedings, 8th International Particle Accelerator Conference (IPAC 2017): Copenhagen, Denmark, May 14–19, 2017, J. Phys. Conf. Ser. 874 (1) (2017) 012004, http://dx.doi.org/10.1088/1742-6596/874/1/012004,10.18429/JACoW-IPAC2017-TUPVA004, [TUPVA004(2017)].

[14] L. Gonzalez, et al., Results on the FCC-hh beam screen sawtooth at the kit electron storage ring kararesults on the Fcc-Hh beam screen sawtooth at the kit electron storage ring kara, in: Proc. 10th International Particle Accelerator Conference, IPAC'19, Melbourne, Australia, 19–24 May, 2019, http://dx.doi.org/10.18429/JACoW-IPAC2019-TUPMP036.

[15] G. Von Holtey, W. Niessen, P. Roudeau, Synchrotron Radiation Masks for LEP2, CERN-SL-94-23-EA, 1994, URL http://cds.cern.ch/record/266590, Jun.

[16] P. Lepeule, C. Menot, R.J.M. Veness, Design and Implementation of Synchrotron Radiation Masks for LEP2, CERN-LHC-96-008-VAC, 1996, URL http://cds.cern.ch/record/307861, CERN-LHC-96-008-VAC.

[17] H.-J. Hagemann, W. Gudat, C. Kunz, Optical constants from the far infrared to the x-ray region: Mg, Al, Cu, Ag, Au, Bi, C, and Al_2O_3, J. Opt. Soc. Amer. 65 (6) (1975) 742–744, http://dx.doi.org/10.1364/JOSA.65.000742.

[18] J.R. Rumble, Handbook of Chemistry and Physics, Taylor and Francis, Chemical Rubber Co, Boca Raton, FL, 2019, URL http://cds.cern.ch/record/244291.

[19] M.N. Polyanskiy, Refractive index database, 2020, URL https://refractiveindex.info. (Accessed 14 July 2020).

[20] A. Latina, E. Adli, B. Dalena, D. Schulte, J. Snuverink, Improvements in the Placet tracking code, Conf. Proc. (2012) 3, URL http://cds.cern.ch/record/1463325, C1205201, (CERN-ATS-2012-166), MOPPC073.

[21] R. Kersevan, M. Ady, Recent developments of Monte–Carlo codes molflow+ and synrad+, in: Proc., 10th International Particle Accelerator Conference, Melbourne, Australia, May 19–24, 2019, http://dx.doi.org/10.18429/JACoW-IPAC2019-TUPMP037.

[22] S. Agostinelli, J. Allison, K. Amako, J. Apostolakis, H. Araujo, P. Arce, M. Asai, D. Axen, S. Banerjee, G. Barrand, F. Behner, L. Bellagamba, J. Boudreau, L. Broglia, A. Brunengo, H. Burkhardt, S. Chauvie, J. Chuma, R. Chytracek, G. Cooperman, G. Cosmo, P. Degtyarenko, A. Dell'Acqua, G. Depaola, D. Dietrich, R. Enami, A. Feliciello, C. Ferguson, H. Fesefeldt, G. Folger, F. Foppiano, A. Forti, S. Garelli, S. Giani, R. Giannitrapani, D. Gibin, J.G. Cadenas, I. González, G.G. Abril, G. Greeniaus, W. Greiner, V. Grichine, A. Grossheim, S. Guatelli, P. Gumplinger, R. Hamatsu, K. Hashimoto, H. Hasui, A. Heikkinen, A. Howard, V. Ivanchenko, A. Johnson, F. Jones, J. Kallenbach, N. Kanaya, M. Kawabata, Y. Kawabata, M. Kawaguti, S. Kelner, P. Kent, A. Kimura, T. Kodama, R. Kokoulin, M. Kossov, H. Kurashige, E. Lamanna, T. Lampén, V. Lara, V. Lefebure, F. Lei, M. Liendl, W. Lockman, F. Longo, S. Magni, M. Maire, E. Medernach, K. Minamimoto, P.M. de Freitas, Y. Morita, K. Murakami, M. Nagamatu, R. Nartallo, P. Nieminen, T. Nishimura, K. Ohtsubo, M. Okamura, S. O'Neale, Y. Oohata, K. Paech, J. Perl, A. Pfeiffer, M. Pia, F. Ranjard, A. Rybin, S. Sadilov, E.D. Salvo, G. Santin, T. Sasaki, N. Savvas, Y. Sawada, S. Scherer, S. Sei, V. Sirotenko, D. Smith, N. Starkov, H. Stoecker, J. Sulkimo, M. Takahata, S. Tanaka, E. Tcherniaev, E.S. Tehrani, M. Tropeano, P. Truscott, H. Uno, L. Urban, P. Urban, M. Verderi, A. Walkden, W. Wander, H. Weber, J. Wellisch, T. Wenaus, D. Williams, D. Wright, T. Yamada, H. Yoshida, D. Zschiesche, Geant4—a simulation toolkit, Nucl. Instrum. Methods Phys. Res. A 506 (3) (2003) http://dx.doi.org/10.1016/S0168-9002(03)01368-8.

[23] G. Dugan, D. Sagan, Simulating synchrotron radiation in accelerators including diffuse and specular reflections, Phys. Rev. Accel. Beams 20 (2) (2017) 020708, http://dx.doi.org/10.1103/PhysRevAccelBeams.20.020708.

[24] MADX - methodological accelerator design, 2020, URL http://madx.web.cern.ch/madx/. (Accessed 14 July 2020).

[25] M. Aicheler, P. Burrows, M. Draper, T. Garvey, P. Lebrun, K. Peach, N. Phinney, H. Schmickler, D. Schulte, N. Toge, A Multi-TeV Linear Collider based on CLIC Technology: CLIC Conceptual Design Report, CERN Yellow Report, CERN, 2012, http://dx.doi.org/10.5170/CERN-2012-007, URL http://cds.cern.ch/record/1500095.

[26] F. Mirapeix, J. Al, J. Amores, J. Presa, A. Urzainki, High precision manufacturing for LINAC's, in: Proc., 27th Linear Accelerator Conference, LINAC2014, Geneva, Switzerland, August 31–September 5, 2014, URL http://jacow.org/LINAC2014/papers/tupp077.pdf.

[27] M. Ady, Monte Carlo Simulations of Ultra High Vacuum and Synchrotron Radiation for Particle Accelerators (Ph.D. thesis), 2016, URL http://cds.cern.ch/record/2157666, Presented 03 May.

[28] G. Guillermo, D. Sagan, F. Zimmermann, Examining mitigation schemes for synchrotron radiation in high-energy hadron colliders, Phys. Rev. Accel. Beams 21 (2) (2018) http://dx.doi.org/10.1103/PhysRevAccelBeams.21.021001.

[29] A.M. Nurnberg, D. Dannheim, Requirements for the CLIC Tracker Readout, CLICdp-Note-2017-002, 2017, URL http://cds.cern.ch/record/2261066.

[30] D. Arominski, A. Sailer, A. Latina, Beam-Induced Backgrounds in CLICdet, CLICdp-Note-2019-007, 2019, URL https://cds.cern.ch/record/2704642.

[31] D. Dannheim, A. Sailer, Beam-Induced Backgrounds in the CLIC Detectors, LCD-Note-2011-021, 2012, URL http://cds.cern.ch/record/1443516.

[32] Y. Bar-Cohen, Low Temperature Materials and Mechanisms, Taylor and Francis, Boca Raton, FL, 2016, http://dx.doi.org/10.1201/9781315371962.

[33] P.E. Liley, Emissivity of solids, in: Heat Exchanger Design Handbook, Department of Chemical Engineering, Imperial College London, UK, http://dx.doi.org/10.1615/hedhme.a.000530.

[34] Engineering ToolBox (2003), convective heat transfer, 2020, URL https://www.engineeringtoolbox.com/convective-heat-transfer-d_430.html. (Accessed 14 July 2020).

[35] J.C. Billy, J.P. Bonon, B. Henrist, N. Hilleret, J.M. Jiménez, I. Laugier, P.M. Strubin, The pressure and gas composition evolution during the operation of the LEP accelerator at 100 GeV, Vacuum 60 (1–2) (2001) 183–189, http://dx.doi.org/10.1016/S0042-207X(00)00383-3.

[36] R. Kersevan, C. Garion, Design of the vacuum system of the FCC-ee electron-positron collider, in: Proc. 10th International Particle Accelerator Conference, IPAC2019, Melbourne, Australia, May 19–24, 2019, 2019, http://dx.doi.org/10.18429/JACoW-IPAC2019-TUPMP035.

[37] O. Groebner, Dynamic Outgassing, CERN-OPEN-2000-275, 1999, http://dx.doi.org/10.5170/CERN-1999-005.127.

[38] D. Arominski, A. Latina, A. Sailer, D. Schulte, Synchrotron radiation reflections in the CLIC beam delivery system, in: Proc. 10th International Particle Accelerator Conference, IPAC'19, Melbourne, Australia, 19–24 May, 2019, http://dx.doi.org/10.18429/JACoW-IPAC2019-WEPTS104.

[39] R. Valizadeh, O.B. Malyshev, S. Wang, T. Sian, M.D. Cropper, N. Sykes, Reduction of secondary electron yield for E-cloud mitigation by laser ablation surface engineering, Appl. Surf. Sci. 404 (2017) 370–379, http://dx.doi.org/10.1016/j.apsusc.2017.02.013.

[40] Y. Wang, et al., Establishing a laser treatment to suppress the secondary electron emission, in: Proc. 10th International Particle Accelerator Conference, IPAC'19, Melbourne, Australia, 19–24 May, 2019, http://dx.doi.org/10.18429/JACoW-IPAC2019-TUPMP029.

[41] S. Arsenyev, D. Schulte, Modelling wake impedance of a rough surface in application to the FCC-hh beamscreen, in: Proc. 9th International Particle Accelerator Conference, IPAC'18, Vancouver, BC, Canada, April 29–May 4, 2018, http://dx.doi.org/10.18429/JACoW-IPAC2018-MOPMF031.